Science Frontiers
2026, Vol. 7, No. 3, pp. 70–78
https://doi.org/10.11648/j.sf.20260703.13

SciencePG
Science Publishing Group

Research Article

Sol-Gel Assisted Synthesis of FeS/MnS Nanocomposites and Their Structural, Vibrational and Optical Properties

Jyoti Bala Kaundal*, Rajesh Sharma

School of Computing& Intelligent System Department, ITM University Gwalior, Gwalior, India

Abstract

The creation of numerous forms of nanoparticles has resulted from the notable acceleration in the development of nanotechnology. These nanoparticles have a wide range of uses, including medication delivery, cosmetics, water purification, and medicine, electronics, and contrast agents for magnetic resonance imaging (MRI), among others. Magnetic materials at the nanoscale size scale have been the focus of significant scientific effort globally for more than half centuries/MnS magnetic nanoparticles were synthesized by sol gel and ultrasonic technique. FeS/MnS magnetic properties of the nanoparticles are obtained by x-ray diffractometry (XRD), UV - visible spectroscopy and Fourier Transform Infrared Spectroscopy we observed in sample on the doping of MnS in Fes nanoparticles. The MnS pure sample absorption is large, and absorption decreases on the increasing concentration of MnS in Fes. It has different obtained the energy band gap of very high here, 3.31 eV, 3.75 eV, 4.71 eV, 4.99 eV and 5.11 eV. In this dissertation, the optical and electrical properties of FeS/MnS magnetic nanoparticles of materials are discussed.

Keywords

FeS/MnS Nanoparticles, Magnetic Properties, Sol-Gel Synthesis, Ultrasonic Technique, XRD, UV-Visible Spectroscopy, FTIR, Energy Band Gap

1. Introduction

The rapid expansion of portable electronics, electric and hybrid electric vehicles, renewable-energy systems, and smart electronic devices has created a growing demand for efficient, reliable, and sustainable energy-storage technologies. Conventional batteries offer relatively high energy density but are generally limited by slower charge-discharge rates and restricted power delivery. In contrast, supercapacitors have emerged as attractive electrochemical energy-storage devices because of their high power density, rapid charge-discharge capability, long operational life, excellent rate performance, and comparatively good cycling stability [1-3]. These characteristics make supercapacitors promising candidates for applications ranging from regenerative braking and portable electronics to backup power systems and renewable-energy integration.

Based on their charge-storage mechanism, supercapacitors are broadly classified into electric double-layer capacitors (EDLCs) and pseudo capacitors [4]. EDLCs store electrical energy primarily through the reversible electrostatic accumulation of ions at the electrode/electrolyte interface, whereas pseudo capacitors involve fast and reversible Faradaic redox

*Correspondence: Jyoti Bala Kaundal (kaundal.jyoti@gmail.com)

Received: 31 August 2026; **Accepted:** 10 September 2026; **Published:** 27 September 2026

reactions. Because pseudocapacitive materials can provide a greater contribution from Faradaic charge storage, they generally offer higher specific capacitance than conventional EDLC materials [4, 5]. Consequently, considerable research has focused on the development of transition-metal-based electrode materials with suitable redox activity, high electrical conductivity, abundant active sites, and favorable ion-transport characteristics.

Transition-metal sulfides have attracted particular attention as promising functional materials because of their variable oxidation states, rich redox chemistry, relatively high theoretical charge-storage capability, and tunable electronic structures [6, 7]. Compared with several transition-metal oxides, sulfide-based materials can exhibit favorable electrical conductivity and efficient charge-transfer characteristics. Their nanoscale architectures can further increase the electrochemically active surface area and shorten ion-diffusion pathways, thereby improving the utilization of active sites. Recent studies have therefore investigated sulfides of Fe, Mn, Co, Ni, Cu, Zn, and other transition metals for supercapacitors, batteries, photocatalysis, sensors, and related energy-conversion applications [6, 7].

Among these materials, iron sulfide (FeS) is particularly attractive because iron is abundant, inexpensive, and comparatively environmentally benign. FeS possesses multiple iron oxidation states and favorable physicochemical properties, which can contribute to reversible Faradaic reactions and charge-storage processes. Nanostructured FeS has demonstrated promising electrochemical behavior and has been investigated as an electrode material for flexible and solid-state supercapacitors [8]. However, the performance of individual FeS nanostructures can be influenced by particle aggregation, limited accessible surface area, structural changes during repeated cycling, and incomplete utilization of electroactive sites. These limitations have motivated the development of FeS-based composite and heterostructured materials.

Manganese sulfide (MnS) represents another important transition-metal sulfide with considerable potential for functional applications. MnS possesses different crystal phases and exhibits attractive physicochemical, optical, and electrochemical properties. Its behavior is strongly influenced by crystal structure, morphology, particle size, defects, and surface characteristics. MnS nanostructures have been investigated as electrode materials for supercapacitors, where their nanoscale morphology can provide accessible active sites and facilitate ion transport [9, 10]. Furthermore, the incorporation of MnS into other functional materials has been reported to modify surface structure, defect concentration, charge-transfer characteristics, and electrochemical activity [11].

The combination of FeS and MnS is particularly interesting because both components belong to the transition-metal sulfide family while providing different physicochemical characteristics. Their integration at the nanoscale can potentially generate interfacial interactions that modify crystallinity, particle size, defect concentration, surface states, and electronic transitions. Such compositional coupling may provide a useful approach for tailoring the properties of FeS-based nanomaterials. A FeS/MnS nanocomposite has previously been investigated as a sodium-ion battery anode and demonstrated improved sodium-storage characteristics compared with the corresponding individual sulfide components, indicating the possibility of beneficial cooperative effects between the Fe-S and Mn-S phases [12]. Related FeS-MnS-containing systems have also been explored for energy-storage applications [13].

Our previous investigations have focused on low-cost synthesis strategies and the characterization of semiconductor and transition-metal chalcogenide nanocomposites. Bala et al. reported stable and reusable tin sulfide-filled cellulose photocatalysts synthesized through a hydrothermal route and demonstrated their application in dye degradation, establishing the potential of sulfide-based nanomaterials for environmental remediation [14]. Subsequently, Kaundal et al. synthesized graphene/ZnO nanocomposites using a low-cost hydrothermal approach and investigated their structural and optical properties [15]. Furthermore, Mohapatra et al. synthesized reduced graphene oxide/zinc sulfide nanocomposites using a sonochemical route and investigated their structural, optical, FTIR, luminescence, and morphological characteristics [16]. This previous work is particularly relevant to the present study because it demonstrates the effectiveness of hydrothermal and ultrasonic-assisted approaches for the preparation of semiconductor and metal-sulfide nanocomposites. Building on this research background, the present work investigates FeS/MnS nanocomposites and examines the influence of MnS incorporation on their structural, vibrational, and optical characteristics.

In addition to their electrochemical relevance, FeS and MnS are interesting from the viewpoint of their optical and electronic properties. The optical absorption of semiconductor sulfides is influenced by crystal structure, crystallite size, defects, surface states, and composition. Consequently, incorporation of MnS into FeS may provide a means of modifying the optical response and band-gap energy of the resulting nanocomposite. X-ray diffraction (XRD) provides information concerning phase formation, crystal structure, and crystallite size, while Fourier-transform infrared (FTIR) spectroscopy can identify characteristic bonding and surface functional groups. UV-visible spectroscopy is useful for evaluating absorption behavior and estimating the optical band gap.

Although FeS- and MnS-based materials have been extensively studied individually and in combination with carbon materials, oxides, and other sulfides, systematic investigations of FeS/MnS nanocomposites prepared by a simple sol-gel route assisted by ultrasonic treatment, particularly with respect to the effect of MnS concentration on their structural and optical properties, remain comparatively limited. Therefore, in the present work, FeS/MnS nanocomposites were synthesized using a sol-gel method assisted by ultrasonic treatment. The influence of MnS incorporation on the structural, vibra-

tional, and optical properties of FeS was systematically investigated using XRD, UV-visible spectroscopy, and FTIR spectroscopy. Particular attention was given to changes in optical absorption and band-gap energy with variation in MnS concentration. The study provides insight into the composition-property relationship of FeS/MnS nanocomposites and establishes a basis for their potential use in future energy-storage, optoelectronic, and other multifunctional applications.

2. Experimental Details

2.1. Materials

All chemicals were of analytical grade and were used as received without further purification. Ferrous chloride, Thiourea (NH_2CSNH_2), MEA as complex agent and liquid Ammonium were all purchased from Aldrich. Glass vessels were cleaned by using multiple cleaning steps with Method

The steps perform in lab for formation of FeS/ MnS nanoparticles.

(A)- Preparation of FeS Nanocomposites.

(B)- Preparation of MnS solution.

(C)- Synthesis of FeS/MnS Nanocomposites.

(A)- Preparation of FeS Nanocomposites using sol gel.

0.1 M molar of $Fecl_3$ dissolved in 80 ml of distilled water and 0.1 M molar thiourea add in it, magnetically stirred for two or three hours. Then add five drops of MEA for complex formation. The variable ratios of $FeCl_3$ and thiourea solutions were used for samples prepared.

$$FeCl3+ H_2O+MEA \rightarrow Fe\ [MEA]^{+2}$$

$$CH_3CSNH_2+H_2\ O \rightarrow s^{+2}+CH_3CN+2H_2O$$

$$Fe[MEA]^{+2} +s^{-2} \rightarrow (Fes)\downarrow+MEA \quad (1)$$

(B)- Preparation of MnS solution

Simultaneously, Mangnese2Chloride solutions were prepared in 80 ml of distilled water in another beaker. Continuously stir for 2 hours. White colored solution will obtained.

$$MnCl2+ H_2O+MEA \rightarrow Mn\ [MEA]^{+2}$$

$$CH_3CSNH_2+H_2\ O \rightarrow s^{+2}+CH_3CN+2H_2O$$

$$Mn[MEA]^{+2} +s^{-2} \rightarrow (Mns)\downarrow+MEA \quad (2)$$

(C)- Synthesis of FeS/MnS Nanocomposites

Water solutions of FeS and mangnese2 chloride were mixed together at molar ratio 1:1, 1:0, 0:1, 1:2 and 2:1. A few drops of ammonia were added to it. Afterwards the solution was transferred onto a magnetic stirrer. Immediately a brown precipitate appeared. When the reaction finished, the stirring was continued for 15 min. The product was several times washed with water and ultrasonicated for 20 min to destroy agglomerates shown in Figure 1.

$$FeS+2MEA+MnS \rightarrow \left(\frac{FeS}{MnS}\right)\downarrow+MEA$$

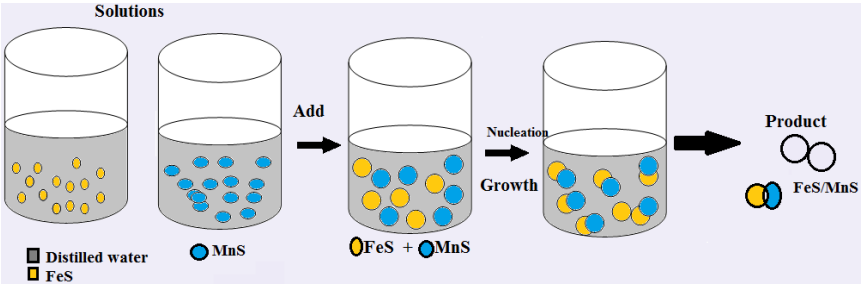

Figure 1. *Flow chart of Synthesis process.*

2.2. Characterizations

The structural studies of FeS/MnS nano-powder were studied by X-ray diffraction measurements (mini Flex 350/600 diffractometer) using the Cu Kα (λ- 1.5406 Å) as a radiation source, scan over the range of 2 °-90 °. The spectral transmittance and absorbance measurements were obtained using UV-VIS spectrometer (Perkin lambda25) in the spectral range of 190 nm to 1100 nm. The X-intercept obtained by extrapolating the linear portion of the exponential curve from of the graph of $(\alpha h\nu)^2$ versus photon energy ($h\nu$) is the bandgap energy of the material. The functional groups and chemical bonding of FeS/MnS nanocomposites were studied by FTIR using Perkin spectrometrum2 from the 500 cm^{-1} to 4000 cm^{-1}. Fluorescence of FeS/MnS nanocomposites were carried out by Perkin Elmer LS-55.

3. Results and Discussions

3.1. Structural Studies (XRD)

The X-ray diffraction (XRD) pattern was recorded using Cu Kα radiation (λ = 1.5406 Å) over the 2θ range of 2-90 °. The

MnS-rich material exhibits diffraction reflections at 2θ = 26.20 °, 28.30 °, 29.80 °, 38.90 °, 46.50 °, 51.00 °, 55.10 °, and 58.40 °. These reflections were assigned in the original analysis to the MnS phase and compared with JCPDS card No. 89-4089. The corresponding interplanar spacings calculated from Bragg's law are approximately 3.399, 3.151, 2.996, 2.313, 1.951, 1.789, 1.665, and 1.579 Å, respectively.

Two additional weak reflections occur near 32.40 ° and 36.20 °. The original manuscript described these peaks as MnO_4; this assignment has been corrected to Mn_3O_4. Published XRD work on MnS indexed with JCPDS No. 89-4089 reports weak reflections near 32.4 ° and 36.1 ° attributable to Mn_3O_4, which may form during preparation because of the complex stoichiometric and oxidation behavior of chalcogenide materials.

The reflections at 33.03 °, 40.91 °, 49.53 °, 57.80 °, 62.55 °, and 64.09° were originally assigned to a card written as "42-13-40" and described as FeS. The correct PDF/JCPDS number is 42-1340, and this card corresponds to pyrite FeS_2 rather than FeS. Literature reports FeS_2 reflections in this region. Therefore, the present XRD evidence supports an FeS_2-containing phase; a definitive FeS assignment should only be retained if independent chemical evidence such as XPS confirms FeS.

The coexistence of MnS-related and FeS_2-related reflections indicates a multiphase sulfide system. Changes in the relative peak intensities with FeS/MnS composition can therefore be discussed as changes in the relative contribution of the crystalline phases. Because FWHM values and raw intensity data are not available in the manuscript, crystallite size should not be reported numerically at this stage. Once FWHM values are obtained, the average crystallite size can be calculated using the Scherrer equation, $D = K\lambda/(\beta \cos\theta)$, where K is approximately 0.89, λ = 1.5406 Å, β is the FWHM in radians, and θ is the Bragg angle.

Table 1. *XRD parameters and crystallite size of the synthesized nanocomposite.*

Phase	2θ (°)	d-spacing (Å)	FWHM (°)	Crystallite size, D (nm)
MnS	26.20	3.399	0.130	62.74
	28.30	3.151	0.166	49.35
	29.80	2.996	0.220	37.37
	38.90	2.313	0.574	14.68
	46.50	1.951	0.150	57.64
	51.00	1.789	0.090	97.80
	55.10	1.665	0.440	20.36
	58.40	1.579	0.430	21.16
Mn_3O_4 (minor)	32.40	2.761	0.393	21.05
	36.20	2.479	0.407	20.54
FeS_2	33.03	2.710	0.393	21.08
	40.91	2.204	0.150	56.53
	49.53	1.839	0.550	15.91
	57.80	1.594	0.110	82.49
	62.55	1.484	0.120	77.46
	64.09	1.452	0.090	104.14

The phase composition and crystalline structure of the synthesized MnS-based nanocomposite were investigated by X-ray diffraction (XRD). The diffraction pattern exhibits distinct reflections corresponding predominantly to MnS, along with weak reflections attributable to secondary phases. The characteristic reflections observed at 2θ = 26.20°, 28.30°, 29.80°, 38.90 °, 46.50 °, 51.00 °, 55.10 °, and 58.40 ° are assigned to the MnS phase based on the corresponding d-spacing values. In addition, weak reflections at 2θ = 32.40° and 36.20° can be indexed to Mn_3O_4, whereas the reflections at 2θ = 33.03°, 40.91 °, 49.53 °, 57.80 °, 62.55 °, and 64.09 °correspond to FeS_2. The coexistence of these reflections confirms the formation of a multiphase MnS/FeS_2-based material with a minor Mn_3O_4 phase the peaks of samples shown in Figure 2A and 2B.

The crystallite size was estimated from the full width at half

maximum (FWHM) of the diffraction peaks using the Scherrer equation, (D = K\lambda/(\beta\cos\theta)), where (D) is the crystallite size, (K) is the shape factor (0.9), (\lambda) is the Cu Kα wavelength (0.15406 nm), (\beta) is the peak broadening in radians, and (\theta) is the Bragg angle. The calculated crystallite sizes for the MnS reflections range from 14.68 to 97.80 nm, reflecting the variation in peak broadening among different crystallographic planes. Based on the major MnS reflections, the crystallite domains are in the nanometer regime, with an approximate mean value of ~45 nm. The relatively broad diffraction peaks indicate the presence of nanoscale crystalline domains, while the coexistence of secondary phases suggests partial phase evolution/oxidation during synthesis. The XRD results therefore confirm the successful formation of the crystalline multiphase nanomaterial.

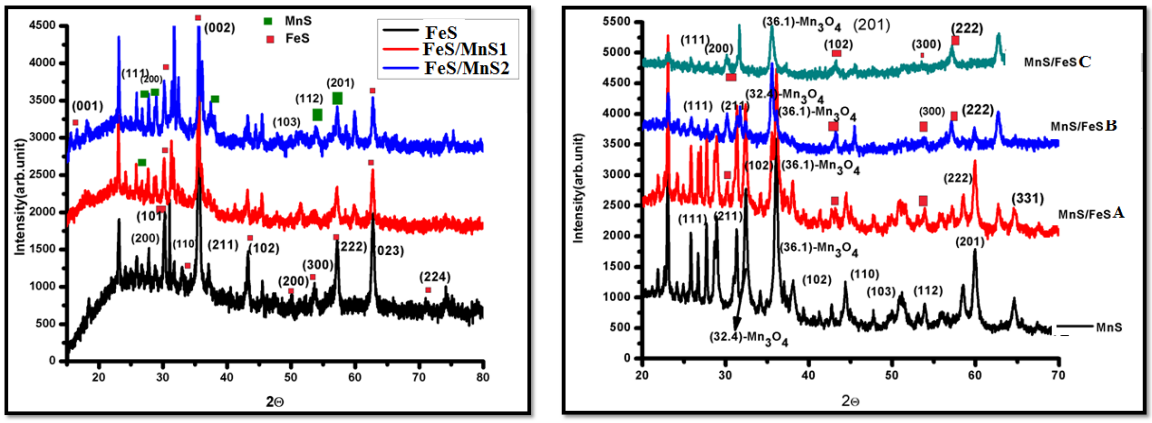

Figure 2. (A). XRD Pattern of FeS/MnS nanocomposites of increasing ratios of MnS in FeS nanoparticles ; (B). XRD pattern of FeS/MnS nanocomposites of increasing ratios of FeS in MnS nanoparticles.

3.2. FTIR

Table 2. FTIR spectra of FeS/MnS nanocomposites showing characteristic functional groups and molecular interactions associated with FeS, MnS, and their nanocomposite.

Wavenumber (cm^{-1})	Tentative assignment	Interpretation
3332-3351	O-H stretching	Surface hydroxyl groups/adsorbed moisture
~3019	Surface C-H/O-H related vibration	Surface-associated species; verify with reagent history
~2793	C-H-related vibration	Surface organic residue
1589-1590	Surface-associated vibration	Adsorbed water/carbon-containing species
1370-1398	Bending vibration	Surface-associated species
~1072	S-O/oxidized sulfur region	Possible surface oxidation; not by itself proof of sulfate
~610	Metal-S vibration region	Consistent with Fe-S/Mn-S bonding contribution

The FTIR spectra were examined to identify the surface chemical environment and characteristic bonding features of the synthesized FeS/MnS nanocomposites. The spectra exhibit bands in the 3332-3351 cm^{-1} region, which can be assigned mainly to O-H stretching associated with surface hydroxyl groups and/or adsorbed moisture. The band near 3019 cm^{-1} and the feature around 2793 cm^{-1} are associated with surface organic/hydrocarbon-related vibrations; their exact assignment should be interpreted together with the synthesis reagents and the corresponding spectra.

A band around 1589-1590 cm^{-1} is observed in the samples and can arise from surface-associated vibrations, including contributions from adsorbed water or carbon-containing surface species. The bands in the 1370-1398 cm^{-1} region may be related to surface bending vibrations. The band near 1072

cm^{-1} is located in a region commonly associated with oxidized sulfur or S-O-containing surface species; therefore, it should not be used alone as evidence for a specific sulfate phase. A lower-wavenumber feature around 610 cm^{-1} lies in the metal-sulfur vibration region and is consistent with bonding contributions from the metal sulfide phases.

The changes in band intensity and position with variation in FeS/MnS composition are significant because they indicate modification of the local surface chemical environment. In particular, any systematic displacement of the low-wavenumber metal-sulfur band can be discussed as evidence of a modified bonding environment at the FeS/MnS interface. The FTIR results therefore complement the XRD results by providing information on local bonding that cannot be obtained from long-range crystal structure alone.

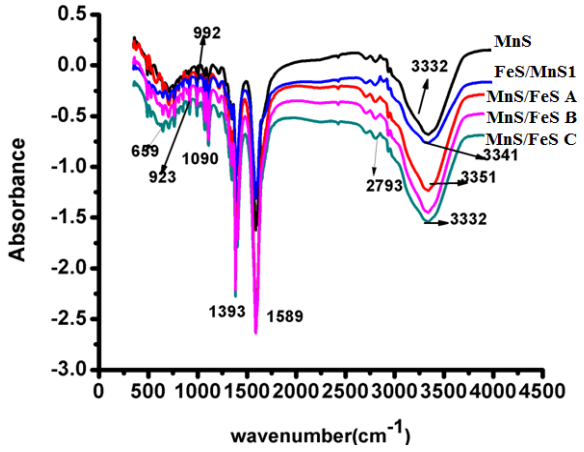

Figure 3. *FTIR peaks of FeS/MnS nanoparticles.*

The intensity of peaks increases on MnS doping O-H stretching vibrations peaks are shown in Figure From 3332, 3341, and 3351 cm-1 some weak stretching of water molecule also present at peak 2793. Below 1000 degree all peaks are attributed as MnS and FeS stretching peaks. The peaks below 600 are assigned as MnS stretching vibrations peaks. The peaks 1589 and 1398 in all samples are C = O, C-H bonding vibrations peaks. Here in this part all information of FTIR characterization had been discussed signally and finally at Figure 3. All plots came at one graph for better understanding and comparing. The FTIR spectroscopy result of FeS_2/MnS nanostructures is shown in Figure 3 OH stretching was seen as a peak at roughly 3300 cm^{-1} and a broad peak centered around 3019 cm^{-1} in this spectrum. The CH bending vibration is represented by the absorption near 1398 cm^{-1}. Furthermore, the band at 1072 cm^{-1} represents the sulphate species' asymmetric S-O stretching. The peak at 610 cm^{-1} was caused by disulfide stretching (S-S), whereas the peak at 610 cm^{-1} was caused by the disulfide stretching (S-S). Infrared spectroscopy was used to acquire vibrational information in order to analyses the chemical bonds and symmetry of molecules.

Also we have two narrow peaks one is due to bending of C = O at 1590 cm^{-1} and the second one is showing the stretching and bending of CO at 1370 $cm^{-1,}$ These are all about FTIR properties of the magnetic nanoparticles.

3.3. UV Spectroscopy

The optical absorption characteristics of the FeS/MnS nanocomposites were evaluated in the UV-visible region to examine the influence of composition on their electronic transitions. The reported spectra show an absorption maximum near 250 nm for the MnS-rich sample, while the FeS-containing sample exhibits an absorption feature near 240 nm and the FeS sample shows an absorption feature around 260 nm. The change in absorption position and intensity with composition indicates that incorporation of FeS and MnS modifies the optical response of the material.

The shift in the absorption region can be associated with changes in the electronic environment produced by coupling of the two sulfide phases. Interfacial interaction between FeS and MnS may alter the distribution of electronic states and surface defects, resulting in a composition-dependent absorption edge. The observed spectral changes should therefore be considered together with the XRD evidence for the coexistence of crystalline sulfide phases and the FTIR evidence for changes in the local chemical environment.

The optical band gap was estimated using the Tauc relationship, $(\alpha h\nu)^2 = A(h\nu - Eg)$, where α is the absorption coefficient, $h\nu$ is the photon energy, Eg is the optical band-gap energy, and A is a proportionality constant. The band-gap value is obtained by extrapolating the linear portion of the Tauc plot to the photon-energy axis. This approach allows the optical response of the individual components and FeS/MnS composites to be compared quantitatively.

The manuscript reports band-gap values of approximately 3.7-3.8 eV for FeS/MnS composite samples, while the reported individual/composition-dependent values include 4.71, 4.99 and 5.11 eV. The abstract also reports a value of 3.31 eV. Because these numerical values are not completely consistent between the abstract and the Results section, the final band-gap values should be taken directly from the original Tauc plots before journal submission. The present discussion therefore retains the reported values without assigning an unsupported final composition-to-Eg trend.

For a clearer presentation, the optical results should be summarized using a sample-wise table containing sample composition, absorption maximum, absorption-edge wavelength, Tauc-plot band gap, and the direction of spectral shift. A plot of Eg against MnS concentration can then be used to demonstrate the composition-optical-property relationship. Such a presentation would make the effect of MnS incorporation much clearer than reporting isolated band-gap values.

The optical results also provide a useful connection between structural and functional properties. Changes in phase composition identified by XRD can modify the electronic

states of the material, while the surface-bonding changes observed by FTIR can influence defect-related absorption. Thus, the UV-visible results support a structure-composition-optical relationship in the FeS/MnS nanocomposite system.

The UV-visible absorption spectra demonstrate a clear dependence of the optical response on FeS/MnS composition. The reported absorption maximum of the MnS-rich sample occurs near 250 nm, whereas the FeS-containing sample shows an absorption feature near 240 nm and the FeS sample exhibits absorption around 260 nm. These changes in absorption position and intensity indicate that incorporation of the second sulfide phase modifies the electronic environment of the nanocomposite.

The observed shift in the absorption edge can be associated with interfacial interaction between the two sulfide components, changes in defect and surface states, and variation in crystallinity and particle size. However, the direction and magnitude of a red or blue shift should be assigned from the actual absorption-edge positions rather than from peak intensity alone. Therefore, the spectra should be compared using both λmax and the absorption-edge wavelength.

The optical band gap was estimated from the Tauc relation, $(\alpha h\nu)^2 = A(h\nu - Eg)$, using the linear region of the plot and extrapolating it to the photon-energy axis. The manuscript reports band-gap values including 3.7-3.8 eV for FeS/MnS composite samples and values of 4.71-5.11 eV for individual/composition-dependent samples. These values must be reconciled with the original Tauc plots before final submission because the abstract and Results section currently contain different numerical sets.

A composition-band-gap relationship should be presented as an additional figure or table. Such a comparison will directly show how MnS incorporation modifies the electronic structure of FeS and will provide a clearer structure-property relationship. The optical results should be interpreted together with XRD and FTIR rather than attributing the band-gap change solely to particle size.

In Figure 4, we observed red shift in Sample on the doping of MnS in Fes Nanoparticles. The MnS Pure Sample absorption is large, and absorption decreases on the increasing concentration of FeS in MnS. And Band gap also increases or decreases with MnS Band Gap can be calculated by using Tauc Plot between Energy hv and $(\alpha h\nu)^2$.

Here the samples showing different absorbance of light at different region, the first sample which its plot shows in the Figure 4 MnS showing a good absorbance at 250 nm and shows 4.9 eV band gap, then in MnS/FeS A, sample that the small ratio of FeS add in MnS, shows a good UV absorption at 240 nm, and the band gap decreases a little from pure MnS on increases the FeS in MnS the band gap is increases and blue shift I obtained on further increases the FeS in MnS but on the other hand, the calculated band gap of pure FeS at 260 nm absorption wavelength is 4.71 eV. When FeS is increases in MnS the ban gap increases as shown in Figure 4. FeS/MnS1 and FeS/MnS2 shows Red shift and the calculated band gap of these samples are 3.8 eV and 3.7 eV.

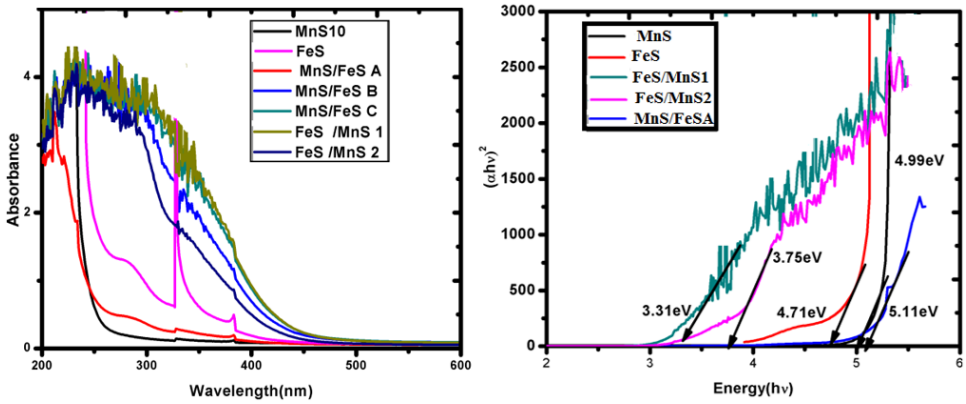

Figure 4. *Shows the different ratios with different band gap.*

Table 3. *Summary of the reported UV-visible optical characteristics of FeS/MnS samples.*

Sample	Composition	Reported λmax (nm)	Reported Eg (eV)	Interpretation
MnS	0:1	~250	~4.9-5.11	Strong UV absorption
FeS/MnS composite	Composite	~240	~3.7-3.8	Composition-dependent optical response
FeS	1:0	~260	~4.71	FeS-related absorption
Reported additional value	Not specified	—	3.31	Must be matched to original Tauc plot

4. Conclusions

In this work, a relatively different and straightforward method for the first time was used for the synthesis of MnS and doping with FeS magnetic nanoparticles. XRD studies shows that the composites have hexagonal wurtizite structures. using conventional methods such as Uv-Vis and FT-IR, the evaluation results of synthesized magnetic nanoparticles confirmed Since we have seen in other articles that the Band gap energy FeS is about 2.7-3.51 electron volts and the Band gap energy MnS is around 3.31 electron volts, we have obtained the energy band gap of very high here, 3.31 eV, 3.75 eV, 4.71 eV, 4.99 eV and 5.11 eV so we conclude that we synthesized these materials very well. As the energy of the band gap increases, the size of the material decreases**.**

Abbreviations

FeS	Iron Sulfide
MnS	Manganese Sulfide
FTIR	Fourier Transform Infrared Spectroscopy
XRD	X-ray Diffraction
UV–Vis	Ultraviolet–Visible Spectroscopy
PL	Photoluminescence
SEM	Scanning Electron Microscopy
TEM	Transmission Electron Microscopy
Eg	Optical Band Gap Energy
FWHM	Full Width at Half Maximum
D	Crystallite Size
2θ	Diffraction Angle
D	Interplanar Spacing

Acknowledgments

The Authors are thankful to ITM University for lab facilities in Nano research lab and also thankful to PC Ray research centre in ITM University Gwalior for providing UV spectroscopy, IR Spectroscopy and Photoluminescence facilities. The authors are thankful to Jiwaji University Gwalior for XRD facilities.

Author Contributions

Jyoti Bala Kaundal: Conceptualization, Data curation, Methodology, Supervision, Visualization, Validation, Writing – original draft, Writing – review & editing

Rajesh Sharma: Investigation, Validation

Conflicts of Interest

The author declares that there are no conflicts of interest associated with this manuscript.

Appendix

Graphical Abstract.

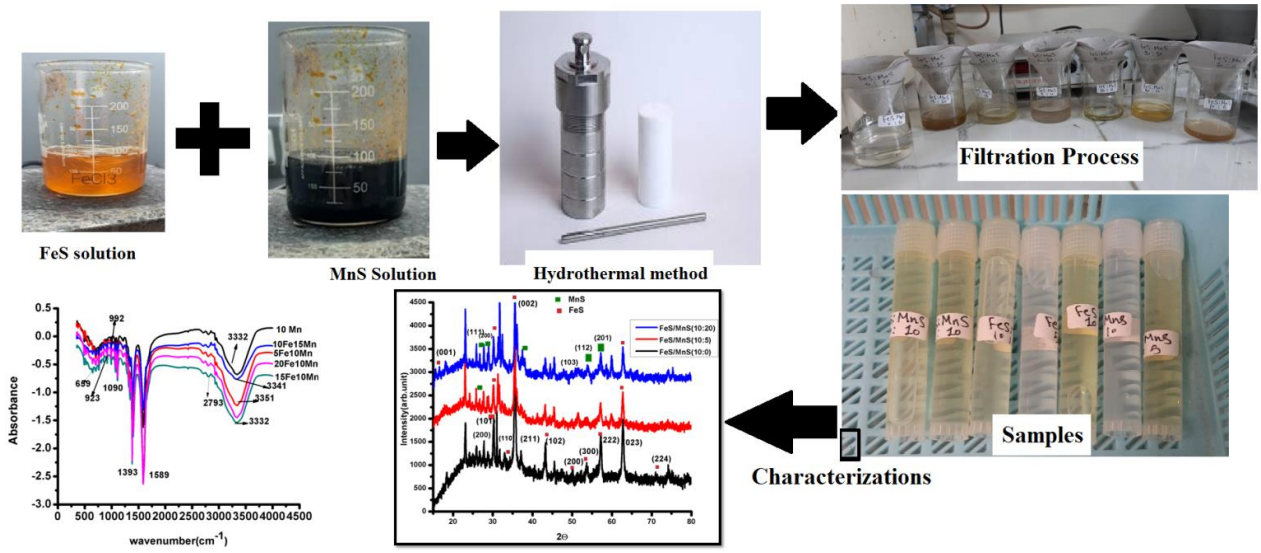

Figure 5. Graphical representation of FeS/MnS magnetic nanoparticle synthesis and characterization.

References

[1] Simon, P., & Gogotsi, Y. (2008). Materials for electrochemical capacitors. Nature Materials, 7, 845-854. https://doi.org/10.1038/nmat2297

[2] Miller, J. R., & Simon, P. (2008). Electrochemical capacitors for energy management. Science, 321, 651-652. https://doi.org/10.1126/science.1158736

[3] Wang, Y., Song, Y., & Xia, Y. (2016). Electrochemical capacitors: Mechanism, materials, systems, and applications. Chemical Society Reviews, 45, 5925-5950. https://doi.org/10.1039/C5CS00580A

[4] Conway, B. E. (1999). Electrochemical Supercapacitors: Scientific Fundamentals and Technological Applications. Kluwer Academic/Plenum Publishers, New York.

[5] Brousse, T., B đanger, D., & Long, J. W. (2015). To be or not to be pseudocapacitive? Journal of The Electrochemical Society, 162, A5185-A5189. https://doi.org/10.1149/2.0201505jes

[6] Kajana, T., Pirashanthan, A., Velauthapillai, D., et al. (2022). Potential transition and post-transition metal sulfides as efficient electrodes for energy storage applications: Review. RSC Advances, 12, 18041-18067. https://doi.org/10.1039/D2RA01574A

[7] Review of Metal Sulfide Nanostructures and their Applications. (2023). ACS Applied Nano Materials. https://doi.org/10.1021/acsanm.3c00417

[8] Karade, S. S., Dwivedi, P., Majumder, S., Pandit, B., & Sankapal, B. R. (2017). First report on a FeS-based 2 V operating flexible solid-state symmetric supercapacitor device. Sustainable Energy & Fuels, 1, 1366-1375. https://doi.org/10.1039/C7SE00165G

[9] Li, L. (2017). One-step synthesis of alpha-MnS nanosheets for supercapacitor electrode materials. Micro & Nano Letters. https://doi.org/10.1049/mnl.2017.0157

[10] All-solid-state high performance asymmetric supercapacitors based on novel MnS nanocrystal and activated carbon materials. (2016). Scientific Reports, 6.

[11] Rajagopal, R., & Ryu, K.-S. (2019). Synthesis of MnO_2 nanostructures with MnS-deposits for high performance supercapacitor electrodes. New Journal of Chemistry. https://doi.org/10.1039/C9NJ02513H

[12] Liu, Q., Zhang, S.-J., Xiang, C.-C., et al. (2019). Rational combination of an alabandite MnS laminated pyrrhotite Fe1−xS nanocomposite as a superior anode material for high performance sodium-ion battery. ACS Sustainable Chemistry & Engineering. https://doi.org/10.1021/acssuschemeng.8b05904

[13] Liu, Q., et al. (2020). Cubic MnS-FeS2 composites derived from a Prussian blue analogue as anode materials for sodium-ion batteries with long-term cycle stability. ACS Applied Materials & Interfaces. https://doi.org/10.1021/acsami.0c10874

[14] Bala, J., Tiwari, R. K., & Goswami, Y. C. (2021). Hydrothermal synthesized stable and reusable tin sulfide filled cellulose photocatalysts and their application in dye degradation. International Journal of Chemical and Biochemical Sciences, 20, 68-70.

[15] Kaundal, J. B., Mohapatra, R., Tiwari, R. K., & Goswami, Y. C. (2022). Low cost hydrothermal synthesis of optically important graphene/zinc oxide nanocomposites. Journal of Ovonic Research, 18(2), 291-299. https://doi.org/10.15251/JOR.2022.182.291

[16] Mohapatra, R., Kaundal, J. B., & Goswami, Y. C. (2021). Synthesis of reduced graphene oxide/zinc sulfide nano composites with sonochemical route. Chalcogenide Letters, 18(5), 255-262. https://doi.org/10.15251/CL.2020.185.255